mAChR5 deficiency disrupts blood-testis barrier and represents a target for modulating male fertility

Running title: mAChR5 controls BTB integrity and male fertility

Weidong Zhang[1,2#], Juanli Huo[1,3#], Yanan Hao[4#], Dongxin Lu[1#], Shen Li[1#], Yukang Li[1#], Xing Qin[1], Xiaolu Wang[1], Jian Tian[1], Feifei Guan[1], Qingyuan Sun[5], Shen Yin[6], Wei Shen[6], Wei Ge[6], Jing Liu[7]*, Bin Yao[1]*, Huiying Luo[1]*, Yong Zhao[1,2]*

[1]State Key Laboratory of Animal Nutrition and Feeding, Institute of Animal Sciences, Chinese Academy of Agricultural Sciences, Beijing 100193, China.

[2]State Key Laboratory of Animal Biotech Breeding, Institute of Animal Sciences, Chinese Academy of Agricultural Sciences (CAAS), Beijing 100193, China.

[3]College of Animal Sciences, Shanxi Agricultural University, Jinzhong 030801, China.

[4]Institute of Brain Science and Brain-inspired Research, Shandong First Medical University and Shandong Academy of Medical Sciences, Jinan 250117, China.

[5]Guangzhou Key Laboratory of Metabolic Diseases and Reproductive Health, Guangdong-Hong Kong Metabolism & Reproduction Joint Laboratory, Reproductive Medicine Center, Guangdong Second Provincial General Hospital, Guangzhou 510317, China.

[6]College of Animal Sciences and Technology, Qingdao Agricultural University, Qingdao 266109, China.

[7]Research Core, Qingdao Agricultural University, Qingdao 266109, China.

[#]These authors contributed equally to this work.

*Corresponding authors.

Email: zhangweidong@caas.cn (W. Zhang), hjllix_0209@163.com (J. Huo), ynhao@sdfmu.edu.cn (Y. Hao), Dx_Lu9812@outlook.com (D. Lu), lishen20192019@outlook.com (S. Li), 821012410055@caas.cn (Y. Li), qinxing@caas.cn (X. Qin), wangxiaolu@caas.cn (X. Wang), tianjian@caas.cn (J. Tian), guanfeifei@caas.cn (F. Guan), sunqy@gd2h.org.cn (Q. Sun), syin@qau.edu.cn (S. Yin), wshen@qau.edu.cn (W. Shen), gewei0901@qau.edu.cn (W. Ge), 201301062@qau.edu.cn (J. Liu), binyao@caas.cn (B. Yao), luohuiying@caas.cn (H. Luo), zhaoyong1688@caas.cn (Y. Zhao).

Abstract

Background: Neuronal signaling is involved in spermatogenesis. The blood-testis barrier (BTB) is the fundamental structure for maintaining spermatogenesis, semen quality, and male fertility. However, how the neuronal signaling modulates the structural integrity and function of BTB, and the underlying mechanisms are poorly understood.

Methods: Using a mouse Sertoli cell (SC) specific knockout approach, muscarinic acetylcholine receptor 5 (mAChR5), a G protein-coupled receptor, was deleted by the Cre-loxP system. The semen quality was quantified by CASA system. The impact on BTB integrity was determined by biotin tracer, transmission electron microscopy (TEM), spatial proteomics, phosphoproteomics, metabolomics, immunofluorescence staining, western blotting analysis.

Results: SC deficiency of mAChR5 disrupts BTB integrity and undermines male fertility. Spatial proteomics analysis revealed that mAChR5 deficiency from SC disturbs phospholipase C (PLC)- protein kinase C (PKC) signaling, subsequently disrupts BTB integrity including the junction proteins gap junction protein alpha 1, tight junction protein 1, occludin, and claudin-11 becoming mislocalized, barrier leakage and increased local oxidative and inflammatory stress. Furthermore, phosphoproteomics analysis discovers that mAChR5-PLC-PKC signaling controls junction protein phosphorylation to maintain BTB integrity, highlighting that BTB integrity is not maintained by static structural components but rather by the dynamic equilibrium between kinase- and phosphatase-mediated remodeling. The impaired BTB integrity upsets the spermatozoa and testicular metabolism to diminish semen quality and male fertility. The identification of a mAChR5–PLC–PKC signaling axis in Sertoli cells advances our understanding of BTB regulation and may provide insights into the mechanisms underlying male reproductive disorders and identify potential therapeutic targets for future investigation.

Conclusion: Pharmacological strategies that selectively preserve mAChR5 activity or downstream PLC-PKC signaling may mitigate the reproductive side effects of environmental factors such as antidepression drugs which adversely impact semen quality through the neuronal pathway.

Keywords: mAChR5; Male fertility; BTB integrity; Cell junction proteins; Protein phosphorylation

Introduction

Male infertility has become a serious global problem [1-4], with sperm concentration and motility continually declining [1]; deleterious impacts include environmental factors [5,6], lifestyle [7-9], and drugs [10] such as antidepressants [11-14]. Sertoli cells represent the principal somatic component of the seminiferous epithelium, forming the blood–testis barrier (BTB) and providing structural and metabolic support essential for germ cell development [15]. Multiple cell junctions (tight, gap, and adherens junctions) collectively form this highly specialized BTB, which divides seminiferous tubules into basal and abluminal compartments [16,17]. The basal compartment provides access to systemic signals and nutrients, whereas the abluminal compartment is immune-privileged and supports meiosis and spermiogenesis, thereby preventing autoimmune rejection of haploid germ cells [16,17]. Regulation of BTB dynamics is orchestrated by both extrinsic modulators (hormones, cytokines, and neurotransmitters) and intracellular signaling pathways (kinases, phosphatases, and calcium-dependent signals) [15-19]. Notably, neurotransmitters such as acetylcholine, glutamate, and monoamines are increasingly recognized as critical modulators of cell junction dynamics, such as tight-junction integrity at the blood–brain barrier (BBB) [20-22]. Given the structural and regulatory parallels between the BBB and BTB, neurotransmitters and neurotrophic factors may also participate in BTB junction regulation.

The neuronal system is integral to spermatogenesis [23,24], and cholinergic fibers regulate steroidogenesis in animal testes [25]. Muscarinic acetylcholine receptors (mAChRs), members of the G protein-coupled receptor (GPCR) family, are present in testes [26] and play crucial roles in male fertility [27-29]. mAChRs1, 3, and 5 mainly couple with Gq/11 to activate the phosphoinositide-specific phospholipase C β (PLCβ) to produce inositol 1,4,5-triphosphate (IP3) and 1,2-diacylglycerol (DAG), followed by the release of intracellular Ca^{2+} and the activation of protein kinase C (PKC) [28,30,31]. mAChR5 has many important roles, making it an attractive therapeutic target [31,32]. Recently, we found that mAChR5 knockdown by shRNA disturbed spermatogenesis through the dysregulation of cell junction proteins [27]. However, how mAChR5 modulates BTB integrity, semen quality and male fertility remains poorly understood. This study uses the cell specific knockout mAChR5 (Sertoli cells or germ cells), spatial proteomics analysis and phosphoproteomics analysis to dissect the roles and

mechanisms of mAChR5 regulating BTB integrity and male fertility.

Results

Sertoli cell mAChR5 deficiency undermines male fertility capacity

To investigate the loss of mAChR5 function in specific testicular cells, we generated mAChR5-flox mice using a CRISPR-Cas9 approach (**Figure S1A-D**). The targeted region within exon 1 contains the entire protein-coding sequence of mAChR5, and the two loxP sites flank this CDS-containing region. Founders that contained the correct insertion in both left and right loxP sites were bred to create homozygous lines. Thus, in the conditional knockout model used in this study, Cre-mediated recombination removes the entire mAChR5 coding sequence while leaving the remaining noncoding portion of exon 1 intact. mAChR5-flox ($mAChR5^{f/f}$) mice were crossed with different Cre lines targeting somatic cells or germ cells in the seminiferous tubules (**Figure S1**): AMH-Cre was used to knock out mAChR5 in Sertoli cells; Stra8-Cre was used to knock out mAChR5 in germ cells especially in spermatogonia cells (SPG). The gene and protein levels of mAChR5 were significantly decreased in SC specific knockout $mAChR5^{\Delta SC}$ ($mAChR5^{f/f}$_AMH-Cre; **Figure S2A-B**), and SPG specific knockout $mAChR5^{\Delta SPG}$ ($mAChR5^{f/f}$_Stra8-Cre; **Figure S2C-D**) compared to $mAChR5^{f/f}$ mice, respectively.

To uncover the impact of Sertoli cell mAChR5 deficiency on fertility, 8-week-age male mouse strains were mated with naïve wild type (WT) female mice (1♂ : 2♀) for one week; pregnancy rate and live pups/litter were determined (**Figure S2E**). Body weight was similar for all four groups at 8 weeks of age (**Figure S2F**); however, testis mass (testis weight/body weight) was significantly less in $mAChR5^{\Delta SC}$ mice than in WT, $mAChR5^{f/f}$, or $mAChR5^{f/+}$_AMH-Cre litter mates (**Figure S2G**). The pregnancy rate was significantly reduced in $mAChR5^{\Delta SC}$ mice (70.0% [42/60]) over WT, $mAChR5^{f/f}$, or $mAChR5^{f/+}$_ AMH-Cre litter mates (85.0% [34/40], 82.5% [33/40], 81.7% [49/60], respectively) (**Figure 1A**). The number of live pups/litter was significantly reduced in $mAChR5^{\Delta SC}$ mice (5.8 ± 1.4 pups/litter, $p < 0.001$) compared with WT, $mAChR5^{f/f}$, and $mAChR5^{f/+}$_AMH-Cre (7.6 ± 1.1, 7.3 ± 1.5, 6.3 ± 1.5 pups/litter, respectively) (**Figure 1B**). Moreover, the sperm motility (a + b + c) was lower in $mAChR5^{\Delta SC}$ mice (69.2 ± 7.0%, $p < 0.001$) over $mAChR5^{f/f}$ (84.3 ± 7.5%) (**Figure 1C**), while sperm abnormality was increased (**Figure S2H**). However, sperm concentration was similar (**Figure S2I**). And the Sertoli cell numbers were similar in $mAChR5^{\Delta SC}$

testes compared to those in mAChR5$^{f/f}$ via immunofluorescence staining (IF) of Sertoli marker SOX9 (**Figure S2J**). But, the testicular germ cells (Marker VASA) were less in mAChR5$^{\Delta SC}$ than that in mAChR5$^{f/f}$ (**Figure S2K**). On the other hand, the body weight and testis mass, sperm motility, concentration and abnormality, pregnancy rate, live pups/litter were similar for mAChR5$^{f/+}$_Stra8-Cre and mAChR5$^{\Delta SPG}$ mice (**Figure S2L-R**). The data indicate that mAChR5 deficiency from Sertoli cells (mAChR5$^{\Delta SC}$) significantly decreased male fertility, but not from germ cells (mAChR5$^{\Delta SPG}$).

Sertoli cell mAChR5 deficiency impairs BTB integrity

To test our hypothesis that mAChR5 deficiency disrupts BTB integrity, a biotin tracer assay was performed [33]. We observed a significant increase in biotin-positive tubules in mAChR5$^{\Delta SC}$ testes compared with mAChR5$^{f/f}$, confirming BTB disruption (**Figure 1D-E**). Consistent with the loss of immune privilege caused by BTB disruption, the levels of anti-sperm autoantibodies were markedly elevated in mAChR5$^{\Delta SC}$ testes compared to mAChR5$^{f/f}$ (**Figure 1F**), further confirming the functionally compromised BTB. Furthermore, BTB ultrastructure was examined by transmission electron microscopy (TEM) at 3, 5, and 8 weeks of age (**Figure 1G**; **Figure S3**).

In 3-week-old mice, the BTB was in the early stages of assembly: adjacent Sertoli cell membranes were closely apposed, tight junctions were visible, and adherens junctions and basal ectoplasmic specializations could be identified (**Figure S3A**). However, electron-dense material associated with the tight junction regions was not yet prominent, indicating immature barrier structures (**Figure S3A**). At 5 weeks of age, the BTB in mAChR5$^{f/f}$ mice was mature and characterized by continuous, electron-dense tight-junction strands aligned along Sertoli cell interfaces (**Figure S3B**). In mAChR5$^{\Delta SC}$ mice, however, structural disruptions were apparent, with discontinuous tight junctions, irregular membrane apposition, and uneven electron-dense material (**Figure S3B**). At 8 weeks of age, these abnormalities were further exacerbated: tight junction strands were fragmented or absent, Sertoli cell membranes were irregular, and basal ectoplasmic specializations were severely disorganized in mAChR5$^{\Delta SC}$ testes. Electron-dense material associated with the junctional regions was markedly reduced, reflecting progressive disruption of BTB architecture (**Figure 1G**; **Figure S3C**).

Subsequently, the expression and localization of BTB junction proteins were analyzed to further validate TEM findings. In mAChR5$^{f/f}$ testes, gap junction proteins alpha 1 (GJA1), tight junction protein 1 (TJP1/ZO-1), occludin (OCLN), and claudin-

11 (CLDN11) displayed strong and continuous localization along the basal compartment of the seminiferous epithelium at 8 weeks (**Figure 1H**). In contrast, mAChR5$^{\Delta SC}$ testes exhibited pronounced disruption and mislocalization of GJA1, OCLN, and CLDN11, while the adherens junction protein N-cadherin (CDH2) appeared diffusely distributed (**Figure 1H**). Western blot analysis further showed a significant reduction in TJP1 protein abundance, whereas OCLN abundance tended to decrease ($p = 0.0917$), and the total protein levels of CLDN11 and CDH2 were not significantly altered **(Figure S4A-B).** Collectively, these findings establish that Sertoli cell–specific deficiency of mAChR5 disrupted both the structural and functional integrity of the BTB, which resulted in barrier leakage, immune activation, and microenvironmental disturbance.

Spatial proteomics unveils mAChR5 deficiency upsetting seminiferous tubular PLC-PKC signaling to impair BTB integrity

To investigate the testicular changes associated with reduced semen quality and male fertility in mAChR5$^{\Delta SC}$ males, we performed histological (H&E) analysis of seminiferous tubules at 1, 3, 5, and 8 weeks of age, covering key stages of postnatal seminiferous epithelial development and BTB establishment (**Figure S5**). We found marked alterations in the seminiferous epithelium of mAChR5$^{\Delta SC}$ testes; the germinal epithelium appeared thinner, the luminal space was expanded, and the number of spermatocytes were notably reduced within the seminiferous epithelium compared with mAChR5$^{f/f}$ mice (**Figure S5E**), suggesting disruption of seminiferous epithelial integrity. To further explore molecular alterations in the testes, we performed spatial proteomic profiling to resolve compartment-specific alterations across the seminiferous epithelium. Seminiferous tubules from mAChR5$^{\Delta SC}$ and mAChR5$^{f/f}$ testes were microdissected and stratified into basal and abluminal region; each compartment was further subdivided into equal-area regions for LC-MS/MS analysis (**Figure 2A**; **Figure S6A**).

The LC-MS/MS analysis achieved considerable proteomic depth, identifying 13,066 peptides (12,716 unique peptides) corresponding to 3,021 proteins, of which 2,866 proteins (94.9%) were retained for quantitative comparison. In the basal compartment, 122 (115 down, 7 up) differentially expressed proteins (DEPs) were identified in mAChR5$^{\Delta SC}$ vs. mAChR5$^{f/f}$ (**Figure 2B**; **Figure S6B**; **Table S1**; **Table S2**). KEGG enrichment analysis showed that DEPs were primarily involved in gap junction,

focal adhesion, cGMP–PKG, WNT, PI3K–AKT, and calcium signaling, and cholinergic synapse, phosphatidylinositol signaling system (**Figure 2C**). Among these networks, PLCβ1, PLCβ3, and PKCα (PRKCA) occupied central regulatory roles (**Figure 2C**). Remarkably, these proteins were interconnected within a common PLCβ–PKC signaling cascade that converged on tight-junction–related pathways, suggesting that a mAChR5–PLCβ–PKC axis may help maintain BTB integrity (**Figure 2C**).

Immunofluorescence staining (IF) was next performed to validate proteomic findings and visualize the spatial distribution of key signaling molecules, including PLCβ1, PLCβ3, and PKCα (**Figure 2D**). In mAChR5$^{f/f}$ testes, PLCβ1 and PLCβ3 exhibited relatively uniform cytoplasmic localization throughout the seminiferous epithelium (**Figure 2D**); however, their fluorescence intensity was markedly reduced, particularly within the basal compartment of mAChR5$^{\Delta SC}$ testes (**Figure 2D**). PKCα displayed a distinct distribution pattern in mAChR5$^{f/f}$ testes; signals were mainly confined to the outermost cell layer, consistent with expression in Sertoli cells and undifferentiated spermatogonia (**Figure 2D**). However, in mAChR5$^{\Delta SC}$ testes, PKCα expression was substantially weaker and its linear basal localization became discontinuous (**Figure 2D**). Consistent with the IF results, Western blotting of whole-testis lysates further confirmed a marked reduction in total PLCβ3 and PKCα protein levels in mAChR5$^{\Delta SC}$ mice compared with mAChR5$^{f/f}$ (**Figure 2E; Figure S6C-D**), indicating that mAChR5 deficiency alters their spatial distribution and reduces their overall testicular expression levels. These observations suggest that loss of mAChR5 suppressed the expression of PLCβ1, PLCβ3, and PKCα within the basal compartment, implying disruption of the canonical mAChR5-PLC-PKC signaling axis [28]. Given that PLCβ hydrolyzes phosphatidylinositol 4,5-bisphosphate (PIP_2) to generate inositol 1,4,5-trisphosphate (IP_3) and diacylglycerol (DAG)—two classical second messengers involved in intracellular Ca^{2+} release and PKC activation [34,35], we next measured total calcium content in spermatozoa and testes after mAChR5 deletion. Total calcium content was significantly reduced in testicular tissue from mAChR5$^{\Delta SC}$ mice, whereas spermatozoa showed a decreasing trend that did not reach statistical significance ($p = 0.0840$) compared with mAChR5$^{f/f}$ mice **(Figure S6E-F)**. We further examined the expression of several calcium-related proteins. ATP2B4 (plasma membrane calcium-transporting ATPase 4), PPP3CC (calcineurin catalytic subunit gamma), and calmegin (CLGN) showed varying degrees of downregulation in mAChR5$^{\Delta SC}$ testes (**Figure 2F-G; Figure S6G-H**). Together with the changes in total calcium content, these results indicate alterations in calcium-related molecular features following Sertoli cell

mAChR5 deficiency [16,34].

However, the levels of proteins in the abluminal compartment exhibited an overall upregulated trend (109 DEPs [22 down, 87 up]) in mAChR5$^{\Delta SC}$ compared with mAChR5$^{f/f}$ (**Figure 3A**; **Table S1; Table S2**). KEGG enrichment analysis revealed significant associations with immune- and stress-related signaling pathways, including the B and T cell receptor signaling pathways, glutathione metabolism, calcium signaling, and pathways of neurodegeneration, ferroptosis, and others (**Figure 3B**). Several immune-related proteins, including interleukin-4-induced 1 (IL4I1), immunoglobulin heavy constant gamma 2B (IGHG2B), COP9 signalosome subunit 2 (COPS2), and toll-interacting protein (TOLLIP), displayed marked alterations (**Figure 3C**). Previous studies suggested that IL4I1 may modulate local immune tolerance by regulating T-cell activation, raising the possibility that its dysregulation contributed to the abluminal immune activation. Therefore, IL4I1 was validated by IF (**Figure 3D**) and Western blotting (**Figure 3E,F**). Moreover, oxidative stress-related proteins, including GPX4, SOD2, and catalase (CAT), were significantly upregulated (**Figure 3D-F**). Moreover, IF staining revealed spatial redistribution of these proteins: CAT increased predominantly in the basal compartment, while GPX4 and SOD2 were more strongly expressed in the abluminal compartment (**Figure 3D**). These spatially distinct protein changes likely represent different but interconnected aspects of seminiferous epithelial dysfunction, with the basal compartment primarily showing alterations in BTB-associated signaling and junctional homeostasis, whereas the abluminal compartment exhibited more prominent immune- and stress-related changes. The cumulative data hereby suggests that Sertoli cells mAChR5 deficiency disrupted the canonical mAChR5-PLC-PKC-signaling pathway. Moreover, mAChR5 deficiency disturbed redox system balance in seminiferous tubules, indicating perturbation of BTB integrity in mAChR5$^{\Delta SC}$ testes.

Phosphoproteomics reveals altered cell junction protein phosphorylation associated with impaired PLC–PKC signaling

PKC serves as a pivotal downstream effector of muscarinic receptor signaling, translating upstream PLCβ signals into phosphorylation events that regulate diverse biological events, including gene expression, cell proliferation, and immune responses [28,35]. Given that mAChR5 deficiency led to reduced PLCβ expression, diminished PKCα levels, and attenuated intracellular Ca^{2+} signaling, we hypothesized a collective

impairment of phosphorylation homeostasis within the seminiferous epithelium. To investigate how mAChR5 deficiency modulates the phosphorylation regulatory network in the testes, we performed a phosphoproteomics analysis of testicular tissue (**Figure 4A; Table S3 and S4**).

A total of 26,315 phosphorylation sites were identified, among which 7.49% showed significant upregulation and 5.47% exhibited significant downregulation (**Figure 4B**). Volcano plot analysis revealed significant alterations in numerous phosphorylation sites following mAChR5 deficiency, indicating extensive phosphorylation remodeling in mAChR5$^{\Delta SC}$ testes (**Figure 4C**). Further KEGG enrichment analysis revealed that the differentially phosphorylated proteins were predominantly enriched in cell junction-related pathways such as tight junctions and adherens junctions (**Figure 4D**), suggesting that mAChR5 deficiency may primarily upset the phosphorylation regulation of junctional complexes associated with the BTB. We further conducted structural localization analyses of the differential phosphorylation sites in multiple key BTB junction proteins. We revealed that three significantly downregulated phosphorylation sites in OCLN: T54, T64, and T303 (**Figure 4E**). Among these, T54 and T64 are located in the N-terminal cytoplasmic region, while T303 is situated in the C-terminal cytoplasmic region (**Figure 4E**), suggesting that mAChR5 deficiency may affect the phosphorylation status of OCLN's cytoplasmic regulatory domain. The significantly downregulated S899 site in TJP1 (ZO-1) is located near the reported OCLN-binding region (**Figure 4F**), suggesting its potential involvement in regulating the stability of the ZO-1-mediated junction complex. Notably, the S912 site near S899 is highly conserved across humans, mice, rats, and cattle, suggesting that this region may constitute a relatively conserved phosphorylation regulatory domain (**Figure 4F**). In contrast, the S1038 and S1061 sites of TJP2 (ZO-2) were significantly upregulated (**Figure 4G**), both located in the distal C-terminal phosphoregulatory region, suggesting that following mAChR5 deficiency, BTB-associated linker proteins may undergo complex phosphorylation remodeling rather than unidirectional changes. GO enrichment analysis of differentially phosphorylated proteins further revealed their predominant involvement in cytoskeletal organization, cell junction assembly, and barrier-related biological processes (**Figure S7A**). The KSEA analysis revealed a declining trend in PKC-related kinase activity (z-score = −1.18) (**Figure S7B**), suggesting that mAChR5 deficiency may impair PKC-mediated

phosphorylation regulation.

Pharmacological interventions confirm impaired PLC-PKC signaling disrupting cell junction protein phosphorylation dynamics to impair BTB integrity

To further verify whether the observed changes in tight junction protein phosphorylation following mAChR5 deficiency are associated with the mAChR5–PKC signaling pathway, we employed pharmacological interventions in cultured seminiferous tubules *in vitro* (**Figure 5A**). Milameline hydrochloride (MH) is an mAChR agonist, and GO6983 is a PKC inhibitor. The seminiferous tubules derived from mAChR5$^{f/f}$ mice were treated and subsequently subjected to phosphoproteomics analysis. PCA revealed distinct clustering patterns among the mAChR5$^{f/f}$ (f/f), mAChR5$^{f/f}$ treated with MH (f/f + MH), and mAChR5$^{f/f}$ treated with GO6983 (f/f + GO6983) groups (**Figure 5B**), demonstrating that both mAChR5 activation and PKC inhibition altered the phosphorylation profile characteristics within the seminiferous tubules. Further analysis of the key phosphorylation sites in BTB-related junction proteins revealed that after MH treatment (mAChR5$^{f/f}$_MH), the phosphorylation levels at OCLN_T303, OCLN_T54, and OCLN_T64 were increased, whereas GO6983 treatment (mAChR5$^{f/f}$_GO) reduced these phosphorylation levels (**Figure 5C**). On the other hand, PLCβ3_S474, VIM_Y117, TJP2_S1061, and TJP2_S1038 exhibited relatively limited changes after MH treatment (mAChR5$^{f/f}$_MH), but showed significant increases following GO6983 treatment (mAChR5$^{f/f}$_GO) (**Figure 5C**). The results demonstrate that mAChR5 activation promotes phosphorylation of certain key BTB junction proteins, whereas PKC inhibition produces the opposite effect, indicating that the mAChR5–PLCβ–PKC signaling pathway participates in regulating the phosphorylation homeostasis of tight junction-related proteins.

Furthermore, we analyzed the responses of mAChR5$^{\Delta SC}$ testes to the MH and GO6983 treatment (**Figure 5D**). Compared to mAChR5$^{f/f}$, the phosphorylation sites of the aforementioned key BTB junction proteins exhibited weak or no responses to both MH and GO6983 in mAChR5$^{\Delta SC}$ testes (**Figure 5D**). The results revealed site-specific responses to pharmacological treatment. The phosphorylation signals of OCLN_T54, OCLN_T64, OCLN_T303, and VIM_Y117 showed relatively little variation across the three conditions. In contrast, TJP1_S899 showed a relative increase following GO6983 treatment, whereas TJP2_S1038 and PLCβ3_S474 showed relative decreases. TJP2_S1061 also exhibited a progressive decrease across the control, MH-treated, and

GO6983-treated conditions.

ML375 is a specific mAChR5 inhibitor. And the BTB-associated junction protein phosphorylation status was altered significantly in ML375 treated mAChR5$^{f/f}$ testes (mAChR5$^{f/f}$_ML375) compared to mAChR5$^{f/f}$ testes (**Figure 5E**). On the other hand, ML375 treated mAChR5$^{f/f}$ testes (mAChR5$^{f/f}$_ML375) exhibited high similarity to mAChR5$^{\Delta SC}$ testes for the BTB-associated junction protein phosphorylation (**Figure 5E**). And the BTB-associated junction protein phosphorylation status was significantly different in mAChR5$^{\Delta SC}$ testes compared to mAChR5$^{f/f}$ testes (**Figure 5E**). The results suggest that mAChR5 deficiency attenuates the phosphorylation response of the tight junction proteins to mAChR5 activation or PKC inhibition, further supporting the central role of mAChR5 in this phosphoregulatory network.

Based on phosphoproteomics data, KSEA results, and pharmacological intervention findings, we further established a phosphorylation regulatory network model illustrating how mAChR5 governs BTB integrity (**Figure 5F**). In the network, mAChR5 is the upstream regulatory node, linking the PLCβ–PKC signaling module and further integrating PAK1/4, small GTPases, and cytoskeletal remodeling-related proteins, ultimately regulating the phosphorylation of tight junction components such as OCLN, TJP1, and TJP2. In addition to cell junction proteins themselves, this network encompasses multiple functional modules, including calcium ion homeostasis regulation, kinase activity switching, cytoskeletal dynamic remodeling, and cell junction assembly, elucidating the underlying molecular pathway through which signal transduction abnormalities progressively lead to instability of the tight junctional complexes following mAChR5 deficiency.

The findings of the current study suggest that mAChR5 may maintain the dynamic stability of Sertoli cell junction complexes by coordinating a PLCβ–PKC dependent phosphorylation network, thereby ensuring the integrity of the BTB and normal spermatogenesis (**Figure 5F**).

Impaired BTB integrity disrupts testicular and spermatozoa metabolism and compromises male fertility

Given the above findings, we next sought to determine spermatozoa and testicular metabolomes to delineate microenvironment alterations correlated to the diminished semen quality and male fertility capacity. Because ATP drives spermatozoa motility [16], we first measured total ATP levels in spermatozoa and found that they were

significantly decreased in mAChR5$^{\Delta SC}$ (**Figure 6A**), indicating impaired energy production. We then conducted untargeted metabolomic profiling of spermatozoa and identified 184 (128 down, 56 up) differentially abundant metabolites in mAChR5$^{\Delta SC}$ compared with mAChR5$^{f/f}$ (**Table S5; Figure 6B**). KEGG (Kyoto Encyclopedia of Genes and Genomes) enrichment analysis identified multiple pathways associated with amino acid metabolism (**Figure 6C**).

These findings highlight that amino acid metabolism was markedly altered in mAChR5$^{\Delta SC}$ spermatozoa. Consistent with this, phosphoenolpyruvate levels remained largely unchanged, whereas among the TCA cycle intermediates, citric and malic acids were significantly reduced, while aconitic acid showed a decreasing trend ($p = 0.0775$) in mAChR5$^{\Delta SC}$ spermatozoa (**Figure 6D**). Moreover, given the strong interconnection between amino acid metabolism and the TCA cycle, we mapped amino acids linked to TCA intermediates (**Figure 6E**) and found that most amino acids were markedly decreased in mAChR5$^{\Delta SC}$, reinforcing the notion that disrupted amino acid–TCA coupling contributed to impaired spermatozoa energetics [36,37]. Perturbation of the TCA cycle severely compromises sperm motility, which is highly dependent on mitochondrial ATP production. Together, these data demonstrate that mAChR5 deficiency disrupted amino acid metabolism and the TCA cycle in spermatozoa, leading to reduced ATP production and diminished motility.

The perturbations in spermatozoa metabolic profiling prompted us to assess the testicular metabolic changes. We performed untargeted metabolomic profiles of testicular tissue and identified 509 (263 down, 246 up) differentially abundant metabolites in mAChR5$^{\Delta SC}$ compared with mAChR5$^{f/f}$ (**Table S6; Figure S8A**). KEGG pathway enrichment analysis separated upregulated and downregulated metabolites according to different terms (**Figure S8B**). Among these, glutathione metabolism was particularly affected, indicating impairment of the redox system. Specifically, reduced glutathione (GSH) was markedly decreased, oxidized glutathione (GSSG) was elevated, and the precursors such as γ-glutamylcysteine and L-glycine were reduced, whereas L-isoleucine was upregulated (**Figure S8C**). This imbalance between GSH and GSSG indicated impaired antioxidant capacity, which could compromise the redox homeostasis required to maintain Sertoli–germ cell interactions and protect developing germ cells [16,38]. Together, these observations suggest that mAChR5 deficiency disrupted BTB integrity to disturb the testicular microenvironment to diminish semen

quality and male fertility capacity. The distinct metabolic changes in testicular tissue and spermatozoa likely reflect their different biological functions. Sertoli cell-specific mAChR5 deficiency was associated predominantly with altered glutathione and redox metabolism in the testis, consistent with disruption of the local testicular microenvironment, whereas spermatozoa showed more prominent impairment of TCA cycle metabolism and ATP production, which may contribute more directly to reduced sperm motility.

Discussion

Our study shows that mAChR5 is indispensable for BTB integrity and seminiferous epithelial organization. mAChR5 deficiency resulted in inter-Sertoli junction loss; the junction proteins GJA1, TJP1, OCLN, and CLDN11 became mislocalized, leading to barrier leakage and increased local oxidative and inflammatory stress. Consequent microenvironment disruption impaired sperm energy metabolism, reduced sperm motility, and ultimately compromised male fertility. These results reaffirm the critical role of tight junction proteins in BTB regulation.

Our data establish a previously unrecognized PLCβ–PKCα–tight junction phosphorylation axis downstream of mAChR5 signaling in the testes, which directly links muscarinic receptor activation to junctional remodeling of the BTB. Deficiency of mAChR5 markedly reduced the expression of PLCβ1, PLCβ3, and PKCα, thereby disrupting the upstream signal cascade that normally drives muscarinic receptor–dependent activation of PKC. This mechanism is consistent with findings from non-testicular tissues, where Gq-coupled muscarinic acetylcholine receptors, particularly the mAChR1, 3, and 5 subtypes, activate PLCβ to hydrolyze phosphatidylinositol-4,5-bisphosphate into DAG and IP_3, leading to intracellular Ca^{2+} mobilization and PKC activation. Notably, PKC functions as a serine/threonine kinase that orchestrates phosphorylation events critical for junctional assembly and turnover [20-22]. In our study, phosphoproteomic analysis showed that mAChR5 deficiency disrupted the phosphorylation balance within the testis, with site-specific alterations in multiple BTB-associated proteins. Although these specific sites have not been functionally characterized in the testis, analogous studies in epithelial and cardiac tissues show that PKC-mediated phosphorylation of GJA1 at other serine residues can profoundly influence channel conductance, junctional stability, and internalization dynamics [20-22]. These findings highlight that BTB integrity is not maintained by static structural

components alone but rather by a dynamic equilibrium between kinase- and phosphatase-mediated remodeling. The PLCβ–PKCα pathway acts as a phosphorylation regulator that fine-tunes the adhesive strength and conformational stability of junctional complexes in response to cellular cues. Importantly, our data establish that cholinergic signaling via mAChR5 represents a previously unrecognized upstream modulator of these phosphorylation-dependent junctional dynamics.

Collectively, these findings highlight a broader role of cholinergic signaling in maintaining testicular homeostasis. The mAChR5–PLCβ–PKCα axis may represent an important regulatory pathway linking neurotransmitter signaling to BTB integrity and male reproductive function. Whether pharmacological modulation of neurotransmitter pathways, including chronic antidepressant treatment, can affect BTB integrity through this pathway remains an interesting question for future study.

Methods

Animals

All animals were housed under standard laboratory conditions (12 - h light/dark cycle, temperature 22 ± 2 °C), with unrestricted access to food and water. The experimental procedures were approved by the Animal Care and Use Committee of the Institute of Animal Sciences, Chinese Academy of Agricultural Sciences (IAS2021-246). C57BL/6J mice were available from the Charles River Laboratory. mAChR5-flox (mAChR5$^{f/f}$) mice were generated using a CRISPR-Cas9-mediated genome editing strategy. Testicular cell-specific knockout of mAChR5 was accomplished through the breeding of mAChR5$^{f/f}$ mice with mice carrying each specific Cre strain: AMH-Cre (Sertoli cell) and Stra8-Cre (Germ cell) [39,40]. The resulting heterozygous offspring (mAChR5$^{f/+}$_AMH-Cre, or mAChR5$^{f/+}$_Stra8-Cre) females were backcrossed with mAChR5$^{f/f}$ males to obtain homozygous offspring (mAChR5$^{\Delta SC}$ or mAChR5$^{\Delta SPG}$) for subsequent experiments. Tail tissue was collected for genotyping. Testes from offspring were also harvested for genotype validation and subsequent analyses [30,40].

Genomic DNA was extracted from mouse tail/testis biopsies using a standard DNA extraction kit (9765, TaKaRa). Genotyping of the mAChR5 allele was performed with primers mAChR5-F1 and mAChR5-R1 (**Table S7**). The PCR program consisted of an initial denaturation at 94 ℃ for 3 min, followed by 35 cycles of 94 ℃ for 30 s, 60 ℃ for 30 s, and 72 ℃ for 35 s; and a final extension at 72 ℃ for 5 min. The expected PCR product sizes were 168 bp for the wild-type allele and 291 bp for the

floxed allele, with heterozygotes showing both bands (**Table S7**). Testis-specific deletion of mAChR5 was confirmed using primers mAChR5-F2 and mAChR5-R2, which amplified a 467 bp product from the conditional knockout allele. PCR cycling conditions were identical to those described above. The AMH-Cre transgene was detected using primers AMH-Cre-F and AMH-Cre-R getting a 540 bp product (**Table S7**). The STRA8-Cre transgene was detected using primers STRA8-Cre-F1 and STRA8-Cre-R1, also yielding a 432 bp product under the same PCR cycling conditions (**Table S7**).

Seminiferous tubule culture and pharmacological treatment

Fresh testes were collected from mAChR5$^{f/f}$ and mAChR5$^{\Delta SC}$ mice, and seminiferous tubules were mechanically isolated under sterile conditions and transferred into Dulbecco's Modified Eagle Medium (DMEM) supplemented with 10% fetal bovine serum (FBS) [41]. Tubules were cultured at 37 °C in a humidified incubator containing 5% CO_2. For pharmacological intervention, seminiferous tubules were randomly assigned to different treatment groups. Milameline hydrochloride (MH, Apexbio, B7123-10A), a muscarinic acetylcholine receptor agonist, was at a final concentration of 1.9 μM. GO 6983 (Solarbio, IG1012), a protein kinase C (PKC) inhibitor, was at a final concentration of 10 nM. ML375 (Sigma, SML2728), a selective negative allosteric modulator of mAChR5, was at a final concentration of 7.9 μM. Untreated seminiferous tubules cultured under identical conditions served as controls. Following 2 h of incubation, seminiferous tubules were collected, immediately frozen in liquid nitrogen, and stored at −80 °C until phosphoproteomic analysis. Phosphopeptide enrichment and LC–MS/MS analysis were subsequently performed as described below.

Fertility testing

To evaluate reproductive capacity, sexually mature male mice of different genotypes were mated with naïve females at a 1 : 2 ratio for one week (WT [20 males], mAChR5$^{f/f}$ [20 males], mAChR5$^{f/+}$_AMH-Cre [30 males], mAChR5$^{\Delta SC}$ [30 males], mAChR5$^{f/+}$_Stra8-Cre [20 males], and mAChR5$^{\Delta SPG}$ [20 males]). The females were monitored for pregnancy rate and live pups/litter [42].

Sperm motility and morphology assessment

The sperm were collected from the cauda epididymis at 8-week-age for sperm motility, concentration, abnormality analysis following previously published protocols

[43-46]. Briefly, the cauda epididymides were immersed in high-glucose Dulbecco's Modified Eagle Medium (DMEM, 11965118, Gibco) supplemented with 15% fetal bovine serum (FBS, S9030, Solarbio). Epididymal contents were gently minced with a sterile scalpel and incubated at 37 ℃ for 5 min to allow sperm release. Sperm concentration and motility were determined by the computer-assisted sperm analysis system (CASA; n = 20 per group) [43-46]. Following Papanicolaou staining [47], at least 300 spermatozoa per mouse were examined to determine abnormality rates. In the CASA analysis used in this study, sperm motility was classified into four categories: a, rapidly progressive sperm; b, slowly progressive sperm; c, non-progressive but motile sperm; and d, immotile sperm. a + b + c represents total sperm motility.

Quantitative real-time PCR (RT-qPCR)

Total RNA was extracted from mouse testicular tissues using TRIzol reagent (12183555, Invitrogen) according to the manufacturer's instructions [43-46]. After measuring the RNA concentration and purity, 1 μg of total RNA was reverse-transcribed into cDNA using the PrimeScript RT reagent kit with gDNA Eraser (RR047A, Takara). Quantitative real-time PCR (RT-qPCR) was performed using TB Green Premix Ex Taq II (RR420A, Takara) on a QuantStudio 6 Flex Real-Time PCR System (Applied Biosystems). Each reaction was performed in triplicate. The relative expression level of mAChR5 was normalized to the housekeeping gene GAPDH using the $2^{-\Delta\Delta Ct}$ method. Primer sequences were listed in **Table S7**.

Hematoxylin & eosin (H&E) staining

Mouse testes were fixed in 4% paraformaldehyde at 4 °C for 24 h, dehydrated in graded ethanol, cleared with xylene, and embedded in paraffin. The tissues were sectioned at 5 μm using a rotary microtome (RM2245, Leica). Sections were deparaffinized in xylene, rehydrated through graded ethanol, and rinsed with distilled water. After staining with hematoxylin for 15 min, the sections were differentiated in 1% acid alcohol and blued in water at 45 °C for 5 min. They were then counterstained with eosin for 30 – 60 s, dehydrated, cleared in xylene, and mounted with a neutral mounting medium. Histological images were obtained using a bright-field microscope (80i, Nikon) [43-45].

Assessment of BTB integrity using biotin tracer

To evaluate the integrity of the blood - testis barrier (BTB), a biotin tracer assay was performed as previously described [48]. Briefly, six mice from each group were

anesthetized, and the testes were carefully exposed. A total of 50 μL of EZ-Link™ Sulfo-NHS-LC-Biotin (10 mg/mL; 21335, Thermo) was injected into the interstitial space of the testes using a micro-syringe. After 30 min, the testes were collected and immediately embedded in Tissue-Tek OCT compound (4583, Sakura) and frozen for cryosectioning. Frozen sections (10 μm) were prepared using a cryostat, fixed in 4% paraformaldehyde for 20 min, and washed with phosphate-buffered saline containing 0.1% Tween-20. The sections were then blocked with 15% goat serum and 1% bovine serum albumin in PBS for 1 h at room temperature. Subsequently, the sections were incubated with Alexa Fluor® 568-conjugated streptavidin (S11226, Invitrogen) for 2 h in the dark at room temperature. After washing, the slides were mounted using antifade mounting medium and analyzed using a fluorescence microscope to evaluate the diffusion pattern of the biotin tracer across the seminiferous epithelium.

Transmission electron microscopy (TEM)

For ultrastructural analysis, testes were dissected and cut into ~1 mm^3 pieces and were fixed in 2.5% glutaraldehyde in 0.1 M phosphate buffer (pH 7.4) overnight at 4 °C, washed three times in PBS, and post-fixed in 1% osmium tetroxide for 2 h at room temperature. After rinsing, tissues were dehydrated through a graded ethanol series and embedded in epoxy resin. Ultrathin sections (70 nm) were cut using an ultramicrotome (Leica UC7), stained with uranyl acetate and lead citrate, and examined under a transmission electron microscope (Hitachi, Japan) [49].

Detection of anti-sperm antibodies in testes

Anti-sperm antibody levels were measured using an ELISA kit (MM-0532M1, Meimian) [50]. Testicular tissues (n = 12 per group) were homogenized in PBS and centrifuged at 10,000 × g for 15 min at 4 °C. The supernatants were added to sperm antigen-coated plates and processed according to the manufacturer's instructions. Absorbance was measured at 450 nm, and antibody levels were calculated from a standard curve, normalized to total protein, and expressed as pg/mg protein.

Measurement of ATP levels in spermatozoa

ATP levels in spermatozoa were measured using an ATP assay kit (BC0305-100T/96S, Solarbio) [51]. Freshly isolated sperm were washed with PBS, and 5 × 10^6 cells were collected for each assay. After lysis, samples were centrifuged at 12,000 × g for 5 min at 4 °C, and the supernatants were used for ATP measurement. Luminescence was recorded after reaction with the ATP detection reagent, and ATP

concentrations were calculated from a standard curve. n = 12 per group.

Measurement of calcium ion (Ca^{2+}) content in testes and spermatozoa

Total Ca^{2+} content was determined using a Calcium Assay Kit (S1063S, Beyotime). Spermatozoa (n = 12 per group) were collected from the cauda epididymis, washed, and lysed in assay buffer. Testicular tissues were homogenized in the same buffer and centrifuged at 12,000 × g for 10 min at 4 °C. Supernatants were mixed with o-Cresolphthalein Complexone reagent, and absorbance at 575 nm was measured using a microplate reader (BioTek, USA). Ca^{2+} concentrations were calculated from a standard curve and expressed as μmol/g protein [52].

Spatial proteomics analysis

To investigate protein expression in testicular tissue, laser capture microdissection (LCM) was performed on testis sections [53]. Briefly, testicular tissues were embedded in paraffin and sectioned at 10 μm using a microtome (RM2245, Leica). Sections were stained with hematoxylin and eosin (H&E) and scanned at 20× magnification using a slide scanner (VS200, Olympus). Seminiferous tubules with intact circular structures were manually selected based on the H&E-stained sections. Six individual mice from each group were included as independent biological replicates. To reduce variation associated with different stages of spermatogenesis, we deliberately selected morphologically comparable seminiferous tubules showing active spermatogenesis from both the control and mAChR5 deficient groups, and the same selection criteria were applied to all animals. For each sample, a complete cross-section of a seminiferous tubule was selected, and the central luminal cavity was excluded to minimize interference from non-cellular components. Based on the spatial organization of the seminiferous epithelium, the remaining tissue was further divided into basal and abluminal regions with approximately equal areas for targeted microdissection. This approach minimized contamination from adjacent cellular region and improved the specificity and reproducibility of the subsequent proteomic analysis.

LCM was performed using a PALM MicroBeam system (Zeiss) to collect the selected regions. The isolated samples were lysed, sonicated for 3 min, and heated at 95 °C for 5 min. Proteins were digested overnight at 37 °C with trypsin (50 ng/sample), followed by C18 desalting and vacuum drying. Peptides were reconstituted in 0.1% formic acid and analyzed using a Vanquish Neo UPLC coupled to an Orbitrap Astral mass spectrometer. Chromatographic separation was performed on a self-packed

reversed-phase column (15 cm × 100 μm) at 200 nL/min using an acetonitrile gradient. Full MS spectra were acquired in the Orbitrap at a resolution of 240,000 over range of a 400 - 800 m/z, while MS/MS spectra were recorded in the Astral analyzer following HCD fragmentation. Raw data were processed with DIA-NN (v1.8) against the Mus musculus UniProt database. Trypsin/P was specified as the digestion enzyme with one missed cleavage allowed, and cysteine carbamidomethylation was set as a fixed modification. Peptide and protein identifications were controlled at an FDR < 1% [54,55].

Phosphoproteomics analysis

For each sample, 800 μg of total protein (n = 3 per group) was reduced with 10 mM TCEP at 37 °C for 1 h and alkylated with 40 mM iodoacetamide for 40 min in the dark. After centrifugation, the protein pellets were dissolved in 100 mM TEAB and digested overnight at 37 °C with trypsin at an enzyme-to-protein ratio of 1 : 50. The resulting peptides were vacuum-dried, reconstituted in 0.1% TFA, desalted using HLB columns, and quantified with a peptide assay kit (23275, Thermo). For phosphopeptide enrichment, peptides were incubated with pre-equilibrated magnetic phosphopeptide enrichment beads, followed by a series of gentle washes to remove non-specifically bound peptides. Phosphopeptides were eluted using 80 μL of elution buffer, acidified to pH 3, and freeze-dried. Final samples were desalted using stage-tips and dried again. Equal amounts of enriched phosphopeptides were reconstituted in MS loading buffer and analyzed by DIA-MS on a Thermo Astral mass spectrometer coupled with a Vanquish Neo UHPLC system. Data were acquired in positive ion mode at 2.2 kV using Thermo Xcalibur version 4.7 software [56-59]. To account for changes in total protein abundance, phosphoproteomic data were normalized to the corresponding protein abundance using matched global proteomic data [60]

Untargeted metabolomics analysis

Testicular tissue (n = 10 per group) and sperm samples (n = 6 per group) were subjected to untargeted metabolomic analysis. Samples were extracted with precooled methanol/acetonitrile/water, sonicated, incubated at −20 °C for 1 h, and centrifuged at 14,000 × g for 15 min at 4 °C. The resulting supernatants were vacuum-dried and reconstituted in 50% methanol for LC–MS analysis. Metabolites were analyzed using an ACQUITY UPLC I-Class Plus system (Waters) coupled to a Q Exactive HF-X mass spectrometer (Thermo Fisher Scientific) under positive and negative ionization modes.

Chromatographic separation was performed on an ACQUITY UPLC HSS T3 column (2.1 × 100 mm, 1.8 μm) with 0.1% formic acid in water and acetonitrile as the mobile phases. Raw MS data were processed for peak extraction, alignment, and normalization. Metabolites were annotated according to accurate mass, MS/MS spectra, and database matching against HMDB, METLIN, and KEGG. PCA and PLS-DA were used to assess group differences, and metabolites with VIP > 1 and $p < 0.05$ were defined as differential metabolites [43-46].

Immunofluorescence staining

Paraffin-embedded testicular tissues were cut into 5 μm sections and mounted on poly-L-lysine-coated slides (188105W, Citotest). After baking at 60 °C for 1 h, the sections were deparaffinized, rehydrated through graded ethanol, and rinsed with distilled water. Antigen retrieval was performed in 10 mM citrate buffer (pH 6.0) at 95 °C for 10 min. The sections were then blocked with 5% normal goat serum containing 0.1% Triton X-100 for 1 h at room temperature and incubated with primary antibodies (1 : 150) overnight at 4 °C. After PBS washing, fluorophore-conjugated secondary antibodies were applied for 45 min at 37 °C in the dark. Nuclei were stained with Hoechst 33342 (C0031-10, Solarbio), and the sections were mounted with anti-fade medium (E675011-0010, BBI). Images were acquired using a fluorescence or confocal microscope. All primary and secondary antibodies used in this study are listed in **Table S8** [43-46].

Western blotting

Tissues were lysed in RIPA buffer (P0013B, Beyotime) supplemented with protease and phosphatase inhibitors (P1005, Beyotime). After centrifugation at 12,000 × g for 15 min at 4 °C, the supernatants were collected and protein concentrations were determined using a BCA assay kit (23225, Thermo). Equal amounts of protein (20 - 40 μg) were separated by 10 - 12% SDS-PAGE and transferred onto PVDF membranes (Millipore). Membranes were blocked with 5% BSA in TBST for 1 h at room temperature and incubated with primary antibodies (1:1,000) overnight at 4 °C. After washing, HRP-conjugated secondary antibodies (1:2000) were applied for 1 h at room temperature **(Table S8).** Protein bands were detected using ECL reagent (32209, Thermo) and imaged with a ChemiDoc system (Bio-Rad). Tubulin served as the loading control, and band intensities were quantified using ImageJ. All antibodies are listed in the supplementary materials [43-46].

Statistical analysis

Data distribution was tested by Shapiro–Wilk normality test. Differences between two groups were analyzed using unpaired two-tailed Student's t-test; multiple group comparisons were analyzed by one-way ANOVA with Tukey's post hoc test. Multiple testing corrections (Benjamini–Hochberg) were applied for omics data. Values are expressed as mean ± s.d. unless otherwise specified. A p-value < 0.05 was considered statistically significant.

Acknowledgments: We thank the Research Cores of the Institute of Animal Sciences of Chinese Academy of Agricultural Sciences for providing excellent services. National Natural Science Foundation of China 32070536 and 31772408 (Y.Z.); National Natural Science Foundation of China 32130101 (H.L.); Central Public-interest Scientific Institution Basal Research Fund Y2025YC43 (Y.Z.); Agricultural Science and Technology Innovation Program CAAS-ZDRW202304 (H.L.).

Author contributions: Conceptualization: J.L., B.Y., Y.Z., H.L.; Methodology: W.Z., J.H., Y.H., D.L., S.L., Y.L., J.L.; Investigation: W.Z., J.H., Y.H., D.L., S.L., Y.L., J.L.; Visualization: F.G., Q.S., S.Y., Y.H., Y.L., W.S., W.G.; Funding acquisition: Y.Z., H.L.; Project administration: X.Q., X.W., B.Y., Y.Z., H.L.; Supervision: B.Y., Y.Z., H.L., X.Q., X.W.; Writing – original draft: W.Z., J.H., Y.H., D.L., S.L., J.L., X.Q., X.W., J.T.; Writing – review & editing: B.Y., Y.Z., H.L., Q.S., W.S., W.G.

Data availability

The mass spectrometry-based spatial proteomics data and global proteomics data have been deposited to the ProteomeXchange Consortium (https://proteomecentral.proteomexchange.org) via the iProX partner repository with the dataset identifier: PXD070805 and PXD086600, respectively. The mass spectrometry phosphorylated proteomics data have been deposited to the ProteomeXchange Consortium via the PRIDE partner repository: PXD079581.

Competing interests: None.

AI use: No AI tools have been used in this manuscript.

References

1. Levine H, Jørgensen N, Martino-Andrade A, Mendiola J, Weksler-Derri D, Jolles M, et al. Temporal trends in sperm count: a systematic review and meta-regression analysis of samples collected globally in the 20th and 21st centuries. Hum Reprod Update. 2023; 29: 157–76.
2. Agarwal A, Baskaran S, Parekh N, Cho CL, Henkel R, Vij S, et al. Male infertility. Lancet. 2021; 397: 319–33.
3. Editorial; Focusing on male infertility. Nat Rev Urol. 2024; 21: 61.
4. Eisenberg ML, Esteves SC, Lamb DJ, Hotaling JM, Giwercman A, Hwang K, et al. Male infertility. Nat Rev Dis Primers. 2023; 9: 49.
5. Gore AC, Chappell VA, Fenton SE, Flaws JA, Nadal A, Prins GS, et al. Executive summary to EDC-2: The Endocrine Society's Second Scientific Statement on endocrine-disrupting chemicals. Endocr Rev. 2015; 36: 593–602.
6. Margiana R, Odhar HA, Prasad K, Oghenemaro EF, Rekha MM, Kumawat R, et al. Does outdoor air pollution cause poor semen quality? A systematic review and meta-analysis. BMC Urol. 2025; 25: 50.
7. Afeiche M, Williams PL, Mendiola J, Gaskins AJ, Jørgensen N, Swan SH, et al. Dairy food intake in relation to semen quality and reproductive hormone levels among physically active young men. Hum Reprod. 2013; 28: 2265–75.
8. Jensen TK, Heitmann BL, Jensen MB, Halldorsson TI, Andersson AM, Skakkebæk NE, et al. High dietary intake of saturated fat is associated with reduced semen quality among 701 young Danish men from the general population. Am J Clin Nutr. 2013; 97: 411–8.
9. Sermondade N, Faure C, Fezeu L, Shayeb AG, Bonde JP, Jensen TK, et al. BMI in relation to sperm count: an updated systematic review and collaborative meta-analysis. Hum Reprod Update. 2013; 19: 221–31.
10. Semet M, Paci M, Saïas-Magnan J, Metzler-Guillemain C, Boissier R, Lejeune H, et al. The impact of drugs on male fertility: a review. Andrology. 2017; 5: 640–63.
11. Alsabhan JF, Almalag HM, Alnuaim LA, Albaker AB, Alaseem MM. Evaluating the use of selective serotonin reuptake inhibitors (SSRIs) and male infertility: A critical retrospective study. J Clin Med. 2024; 13: 2129.
12. Rothmore J. Antidepressant-induced sexual dysfunction. Med J Aust. 2020; 212: 329–34.

13. Read J, Williams J. Adverse effects of antidepressants reported by a large international cohort: emotional blunting, suicidality, and withdrawal effects. Curr Drug Saf. 2018; 13: 176–86.
14. Tousson E, Hafez E, Zaki S, Gad A, Elgharabawy RM. Evaluation of the testicular protection conferred by damiana (Turnera diffusa Willd.) against amitriptyline-induced testicular toxicity, DNA damage and apoptosis in rats. Biomed Pharmacother. 2020; 132: 110819.
15. Franca LR, Hess RA, Dufour JM, Hofmann MC, Griswold MD. The Sertoli cell: one hundred fifty years of beauty and plasticity. Andrology. 2016; 4: 189–212.
16. Cheng CY. Molecular mechanisms in spermatogenesis (Landes Bioscience / Springer Science+Business Media, LLC, 2008)
17. Balda MS, Matter K. Tight junctions and the regulation of gene expression. Biochim Biophys Acta. 2009; 1788: 761–7.
18. Mruk DD, Cheng CY. The mammalian blood-testis barrier: Its biology and regulation. Endocr Rev. 2015; 36: 564–91.
19. Luaces JP, Toro-Urrego N, Otero-Losada M, Capani F. What do we know about blood-testis barrier? current understanding of its structure and physiology. Front Cell Dev Biol. 2023; 11: 1114769.
20. Luissint AC, Artus C, Glacial F, Ganeshamoorthy K, Couraud PO. Tight junctions at the blood brain barrier: physiological architecture and disease-associated dysregulation. Fluids Barriers CNS. 2012; 9: 23.
21. Ikuya K, Dohgu S, Takata F, Matsumoto J, Kawahara Y, Nishihira M, et al. Activation of the α7 nicotinic acetylcholine receptor upregulates blood brain barrier function through increased claudin-5 and occludin expression in rat brain endothelial cells. Neurosci Lett. 2019; 694: 9–13.
22. Hawkins RA. The blood-brain barrier and glutamate. Am J Clin Nutr. 2009; 90: 867S–74S.
23. Gerendai I. Supraspinal connections of the reproductive organs: structural and functional aspects. Acta Physiol Hung. 2004; 91: 1–21.
24. Chow SH, Giglio W, Anesetti R, Ottenweller JE, Pogach LM, Huang HF. The effects of testicular denervation on spermatogenesis in the Sprague-Dawley rat. Neuroendocrinology. 2000; 72: 37–45.
25. Zhu C, Palmada MN, Aguado LI, Cavicchia JC. Administration of acetylcholine to

the spermatic nerve plexus inhibits testosterone secretion in an in vitro isolated rat testis-nerve plexus system. Int J Androl. 2002; 25: 134–8.
26. Eglen RM. Muscarinic receptor subtypes in neuronal and nonneuronal cholinergic function. Auton Autacoid Pharmacol. 2006; 26: 219–33.
27. Han X, Zhang C, Ma X, Yan X, Xiong B, Shen W, et al. Muscarinic acetylcholine receptor M5 involved in spermatogenesis through the modification of cell-cell junctions. Reproduction. 2021; 162: 47–59.
28. Porto CS, Lucas TFG, Siu ER, Royer C, Trindade ES, Nader HB, Lazari MFM, et al. Muscarinic acetylcholine receptors: relevance to infertility and male contraception. Immunol Endocr Metab Agents Med Chem. 2008; 8: 42–50.
29. Borges MO, Abreu ML, Porto CS, Avellar MC. Characterization of muscarinic acetylcholine receptor in rat Sertoli cells. Endocrinology. 2001; 142: 4701–10.
30. Bender AM, Garrison AT, Lindsley CW. The muscarinic acetylcholine receptor M5: therapeutic implications and allosteric modulation. ACS Chem Neurosci. 2019; 10: 1025–34.
31. Vuckovic Z, Gentry PR, Berizzi AE, Hirata K, Varghese S, Thompson G, et al. Crystal structure of the M5 muscarinic acetylcholine receptor. Proc Natl Acad Sci USA. 2019; 116: 26001–7.
32. Berizzi AE, Gentry PR, Rueda P, Den Hoedt S, Sexton PM, Langmead CJ, et al. Molecular mechanisms of action of M5 muscarinic acetylcholine receptor allosteric modulators. Mol Pharmacol. 2016; 90: 427–36.
33. Zheng S, Zhao N, Lin X, Jiang L, Qiu C, Jiang J, et al. Fine particulate matter (PM 2.5) and the blood-testis barrier: an in vivo and in vitro mechanistic study. Environ Health Perspect. 2025; 133: 047006.
34. Woll KA, Van Petegem F. Calcium-release channels: structure and function of IP(3) receptors and ryanodine receptors. Physiol Rev. 2022; 102: 209–68.
35. Rhee SG. Regulation of phosphoinositide-specific phospholipase C. Annu Rev Biochem. 2001; 70: 281–312.
36. Becerro RL, Martín CFE, Silva RA, Ortega FC, da Silva ÁE, Gil C, et al. Targeted metabolomics reveals the impact of glucose and pyruvate on energy metabolism and storage potential of stallion spermatozoa. Metabolomics. 2026; 22(2):45.
37. Sexton TJ, Amann RP, Flipse RJ. Oxidative metabolism of glutamate by testicular, epididymal, and ejaculated bovine spermatozoa in the presence of rete testis fluid

and seminal plasma. J Dairy Sci. 1972; 55(7):1005–9.

38. Castellón EA. Glutathione and gamma-glutamyl cycle enzymes in rat testis during sexual maturation. Arch Androl. 1994; 33: 179–85.

39. Lei W, Li Y, Meng T, Ning Y, Sun S, Zhang C, et al. Specific deletion of protein phosphatase 6 catalytic subunit in Sertoli cells leads to disruption of spermatogenesis. Cell Death Dis. 2021; 12: 883.

40. Li N, Yu J, Feng Y, Xu P, Wang X, Zhou M, et al. Conditional ablation of DIS3L2 ribonuclease in pre-meiotic germ cells causes defective spermatogenesis and infertility in male mice. Theranostics. 2024; 14: 5621–42.

41. Zhao Y, Zhang P, Ge W, Feng Y, Li L, Sun Z, et al. Alginate oligosaccharides improve germ cell development and testicular microenvironment to rescue busulfan disrupted spermatogenesis. Theranostics. 2020; 10: 3308–24.

42. Argaw-Denboba A, Schmidt TSB, Di Giacomo M, Ranjan B, Devendran S, Mastrorilli E, et al. Paternal microbiome perturbations impact offspring fitness. Nature. 2024; 629: 652–9.

43. Zhao Y, Zhang W, Liu X, Zhang P, Hao Y, Li L, et al. Hydrogen sulfide and/or ammonia reduces spermatozoa motility through AMPK/AKT related pathways. Sci Rep. 2016; 6: 37884.

44. Zhang W, Zhao Y, Zhang P, Hao Y, Yu S, Min L, et al. Decrease in male mouse fertility by hydrogen sulfide and/or ammonia can be inheritable. Chemosphere. 2018; 194: 147–57.

45. Hao Y, Feng Y, Yan X, Chen L, Zhong R, Tang X, et al. Gut microbiota-testis axis: FMT improves systemic and testicular micro-environment to increase semen quality in type 1 diabetes. Mol Med. 2022; 28: 45.

46. Zhang P, Feng Y, Li L, Ge W, Yu S, Hao Y, et al. Improvement in sperm quality and spermatogenesis following fecal microbiota transplantation from alginate oligosaccharide dosed mice. Gut. 2021; 70: 222–5.

47. Vieira CP, Martins Lara NLE, Procopio MS, Avelar GF: Optimization of spermatozoa analysis in mice: A comprehensive protocol. Tissue Cell. 2024; 89: 102463.

48. Meng J, Holdcraft RW, Shima JE, Griswold MD, Braun RE. Androgens regulate the permeability of the blood-testis barrier. Proc Natl Acad Sci USA. 2005; 102: 16696–700.

822 49. Chemes HE. Ultrastructural analysis of testicular tissue and sperm by transmission
823 and scanning electron microscopy. Methods Mol Biol. 2013; 927: 321–48.
824 50. Zaki AA, Aldahmashi FS, Madboli AEA, Attia KA, Almulhim FS, Albarrak SM.
825 Therapeutic approaches for anti-sperm-antibodies in the testicular sperm
826 aspiration rat model. Vet World. 2023; 16: 296–308.
827 51. Sun Z, Zhang W, Xue X, Zhang Y, Niu R, Li X, et al. Fluoride decreased the sperm
828 ATP of mice through inhabiting mitochondrial respiration. Chemosphere. 2016;
829 144: 1012–7.
830 52. Wennemuth G, Blöcher S, Schill WB, Aumüller G, Monsees TK. Bradykinin
831 increases intracellular calcium levels in rat testis peritubular cells via the B2
832 receptor subtype. Br J Pharmacol. 2003; 138: 351–8.
833 53. Dong Z, Jiang W, Wu C, Chen T, Chen J, Ding X, et al. Spatial proteomics of single
834 cells and organelles on tissue slides using filter-aided expansion proteomics. Nat
835 Commun. 2024; 15: 9378.
836 54. Chen T, Ma J, Liu Y, Chen Z, Xiao N, Lu Y, et al. iProX: an integrated proteome
837 resource. Nucleic Acids Res. 2019; 47(D1): D1211–7.
838 55. Chen T, Ma J, Liu Y, Chen Z, Xiao N, Lu Y, et al. iProX in 2021: connecting
839 proteomics data sharing with big data. Nucleic Acids Res. 2021; 50(D1): D1522–
840 7.
841 56. Blazev R, Carl CS, Ng Y, Molendijk J, Voldstedlund CT, Zhao Y, et al.
842 Phosphoproteomics of three exercise modalities identifies canonical signaling and
843 C18ORF25 as an AMPK substrate regulating skeletal muscle function. Cell Metab.
844 2022; 34: 1561–77.e9.
845 57. Srinivasan A, Sing JC, Gingras AC, Röst HL. Improving phosphoproteomics
846 profiling using data-independent mass spectrometry. J Proteome Res. 2022; 21:
847 1789–99.
848 58. Bortel P, Piga I, Koenig C, Gerner C, Martinez-Val A, Olsen JV. Systematic
849 optimization of automated phosphopeptide enrichment for high-sensitivity
850 phosphoproteomics. Mol Cell Proteomics. 2024; 23: 100754.
851 59. Perez-Riverol Y, Bandla C, Kundu DJ, Kamatchinathan S, Bai J, Hewapathirana S,
852 et al. The PRIDE database at 20 years: 2025 update. Nucleic Acids Res. 2025;
853 53(D1): D543–53.
854 60. Wu R, Dephoure N, Haas W, Huttlin EL, Zhai B, Sowa ME, Gygi SP. Correct

855 interpretation of comprehensive phosphorylation dynamics requires normalization
856 by protein expression changes. Mol Cell Proteomics. 2011; 10(8): M111.009654.

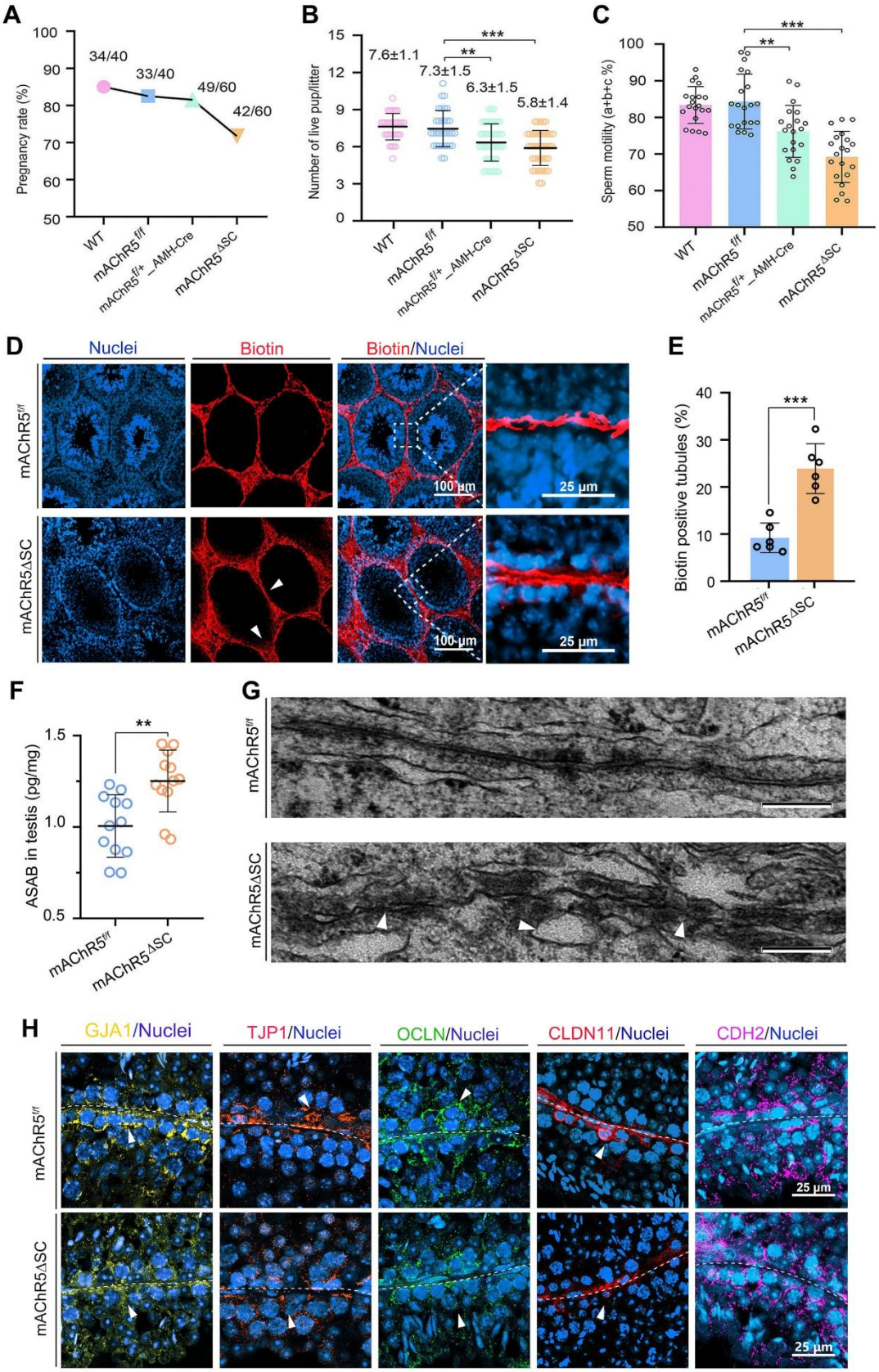


Figure 1. Sertoli cell mAChR5 deficiency diminishes semen quality, male fertility, and disrupts the blood-testis barrier (BTB). (A) The pregnancy rate (the number of

pregnant females versus total females mated; male-to-female ratio of 1 : 2). **(B)** The number of live pups/litter (Mean ± s.d.). **(C)** Sperm motility (a + b + c). n = 20 per group (Mean ± s.d.). **(D)** Biotin tracer assay of BTB permeability in testes. Scale bars, 100 μm for low-magnification images and 25 μm for high-magnification inset images. Arrows indicate infiltration of biotin dye into the seminiferous tubules. n = 6 per group. **(E)** Quantification of biotin-positive seminiferous tubules (Mean ± s.d.). n = 6 per group. **(F)** Immunodetection of anti-sperm autoantibodies (ASAB) in testicular tissue. n = 12 per group. **(G)** Transmission electron microscopy (TEM) images of testicular tight junctions, with arrows marking disrupted junctional structures. Scale bar, 200 nm. **(H)** Immunofluorescence staining of junctional and adhesion proteins GJA1 (yellow), TJP1 (orange), OCLN (green), CLDN11 (red), and CDH2 (purple) in testicular sections. **p < 0.01, ***p < 0.001.

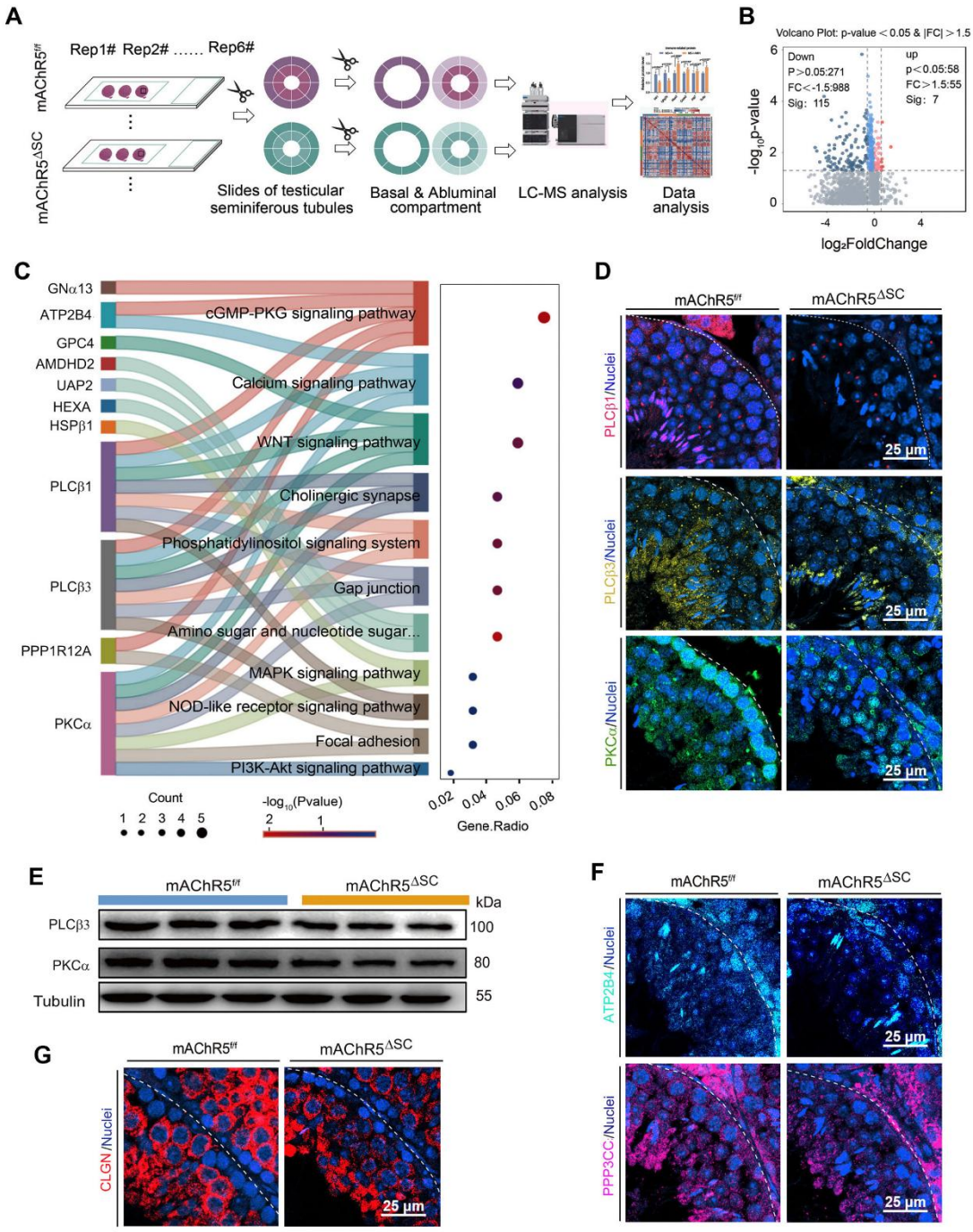
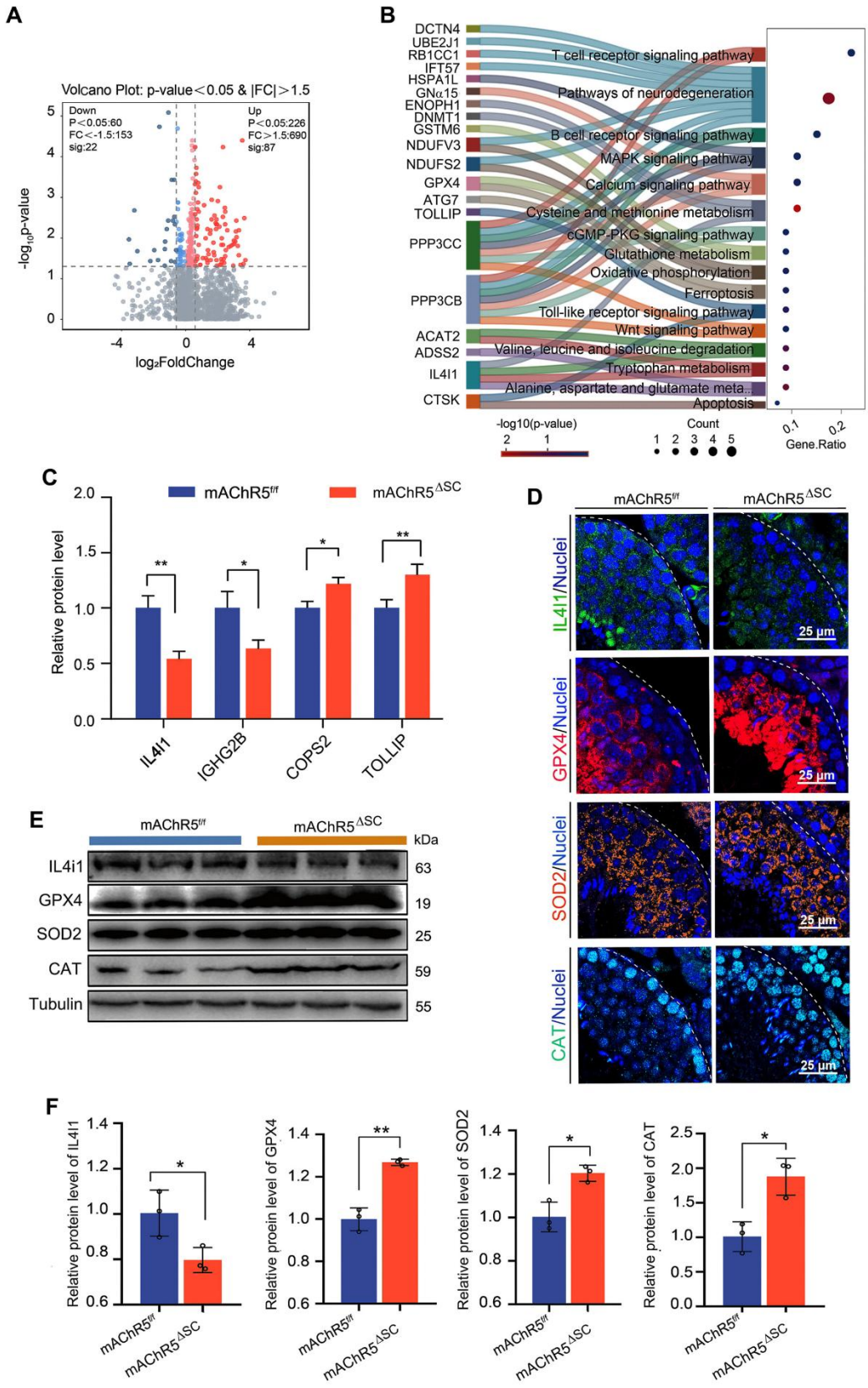


Figure 2. Spatial proteomics identified altered PLC–PKCα signaling in mAChR5-deficient testes. (A) Schematic illustration of the workflow for spatial proteomic analysis. n = 6 per group. **(B)** Volcano plot showing differentially expressed proteins (DEPs) identified in the basal compartment of seminiferous tubules between mAChR5$^{f/f}$ and mAChR5$^{\Delta SC}$ testes. **(C)** KEGG pathway enrichment analysis and a correlation network linking enriched pathways with representative proteins. **(D)** Immunofluorescence staining of PLCβ1 (purple), PLCβ3 (orange), and PKCα (green).

Scale bar, 25 μm. **(E)** Western blotting analysis of PLCβ3 and PKCα protein levels. Tubulin as a loading control. n = 3 per group. **(F)** Immunofluorescence staining of ATP2B4 (light blue), PPP3CC (purple), Scale bar, 25 μm. **(G)** Immunofluorescence staining of CLGN (red), Scale bar, 25 μm.



884

885 **Figure 3. DEPs in the abluminal compartment of seminiferous tubules by spatial**

886 **proteomics. (A)** Volcano plot illustrating DEPs in the abluminal compartment of

seminiferous tubules. **(B)** KEGG pathway enrichment analysis and a correlation network linking enriched pathways with representative proteins. **(C)** Relative protein levels of immune-related differentially expressed proteins, including IL4I1, IGHG2B, COPS2, and TOLLIP. n = 6 per group. **(D)** Immunofluorescence staining of IL4I1, GPX4, SOD2, and Catalase (CAT) in mAChR5$^{f/f}$, mAChR5$^{\Delta SC}$ testes. Scale bar, 25 μm. **(E)** Western blotting of oxidative stress–related proteins IL4I1, GPX4, SOD2, and CAT in mAChR5$^{f/f}$, mAChR5$^{\Delta SC}$ testes. **(F)** Relative protein levels of IL4I1, GPX4, SOD2, and CAT by Western blotting. n = 3 per group. Mean ± s.d. *$p < 0.05$, **$p < 0.01$.

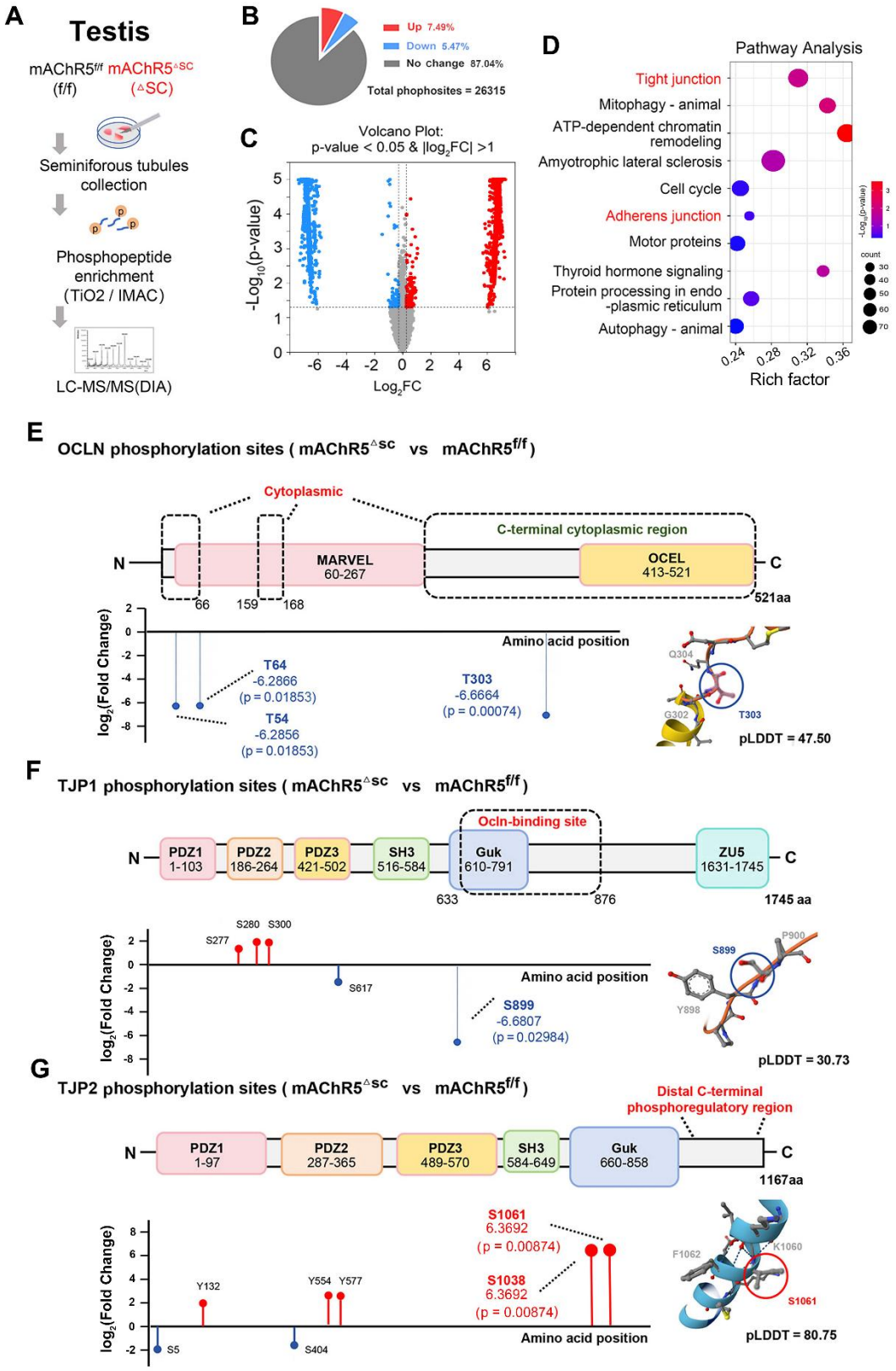


Figure 4. Phosphoproteomics analysis of testes from mAChR5$^{f/f}$ and mAChR5$^{\Delta SC}$ mice. (A) Schematic illustration of the phosphoproteomic workflow. **(B)** Distribution of differentially phosphorylated sites identified in control and mAChR5-deficient testes.

(C) Volcano plot of differentially phosphorylated sites. **(D)** KEGG pathway enrichment analysis of differentially phosphorylated proteins. **(E)** Structural mapping of differentially phosphorylated sites in OCLN. **(F)** Structural mapping of the differentially phosphorylated sites in TJP1. **(G)** Structural mapping of differentially phosphorylated sites in TJP2.

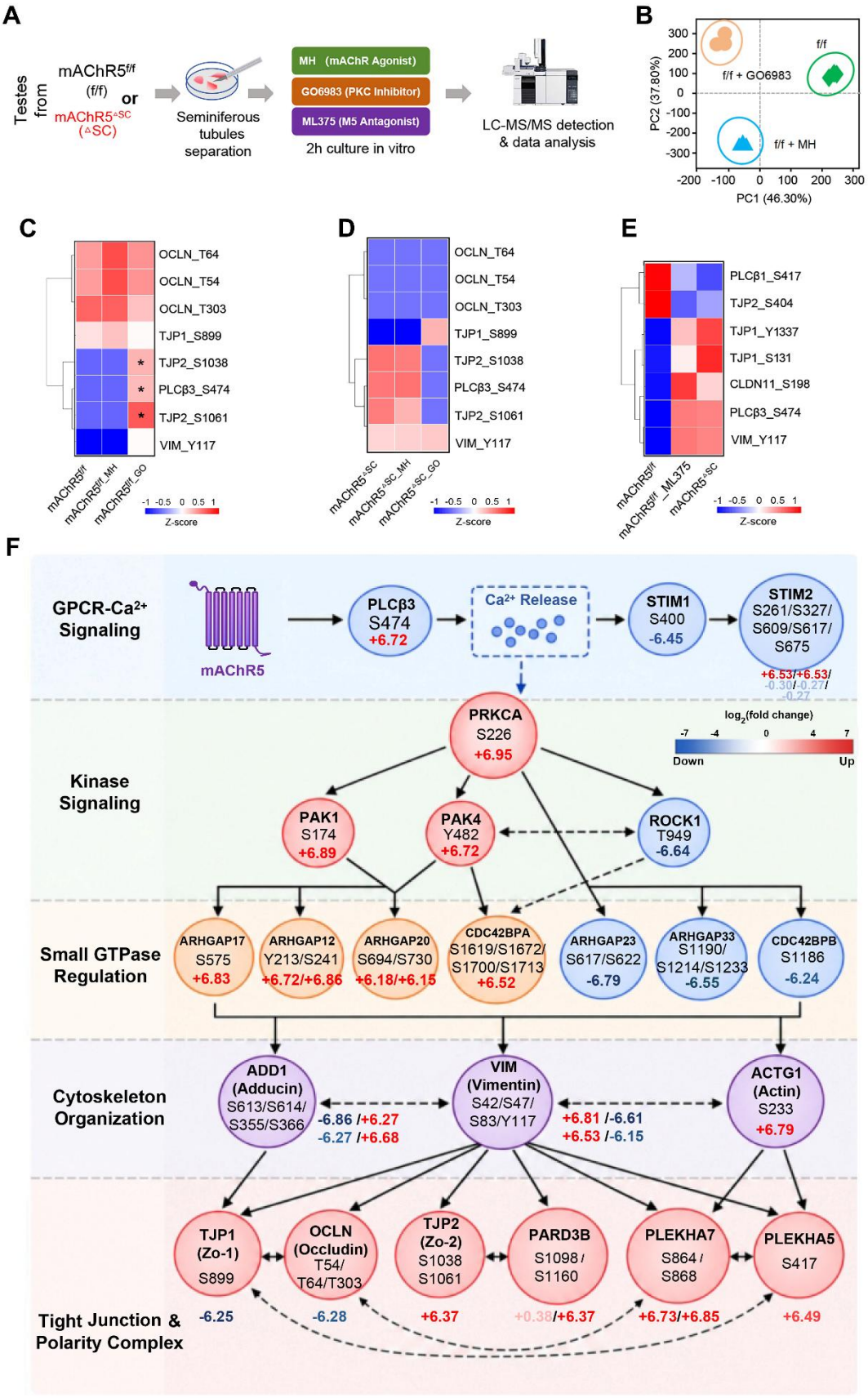


Figure 5. Pharmacological regulation of BTB-associated phosphoproteins and construction of the mAChR5-related phosphoregulatory network. (A)

Experimental design of seminiferous tubule culture and pharmacological treatments. Milameline hydrochloride (MH); GO6983; and ML375. **(B)** Principal component analysis (PCA) of phosphoproteomic profiles from control seminiferous tubules treated with MH or GO (GO6983). **(C)** Phosphorylation levels of representative BTB-associated proteins in mAChR5$^{f/f}$ seminiferous tubules following MH or GO (GO6983) treatment. **(D)** Phosphorylation levels of representative BTB-associated proteins in mAChR5-deficient seminiferous tubules following MH or GO (GO6983) treatment. **(E)** Phosphorylation levels of representative BTB-associated proteins in mAChR5$^{f/f}$, ML375-treated mAChR5$^{f/f}$ (mAChR5$^{f/f}$_ML375), and mAChR5$^{\Delta SC}$ seminiferous tubules. **(F)** Proposed phosphoregulatory network illustrating the role of mAChR5 in regulating BTB integrity. Numbers indicate the $\log_2$(fold change) of the corresponding phosphorylation sites, with identical values shown only once.

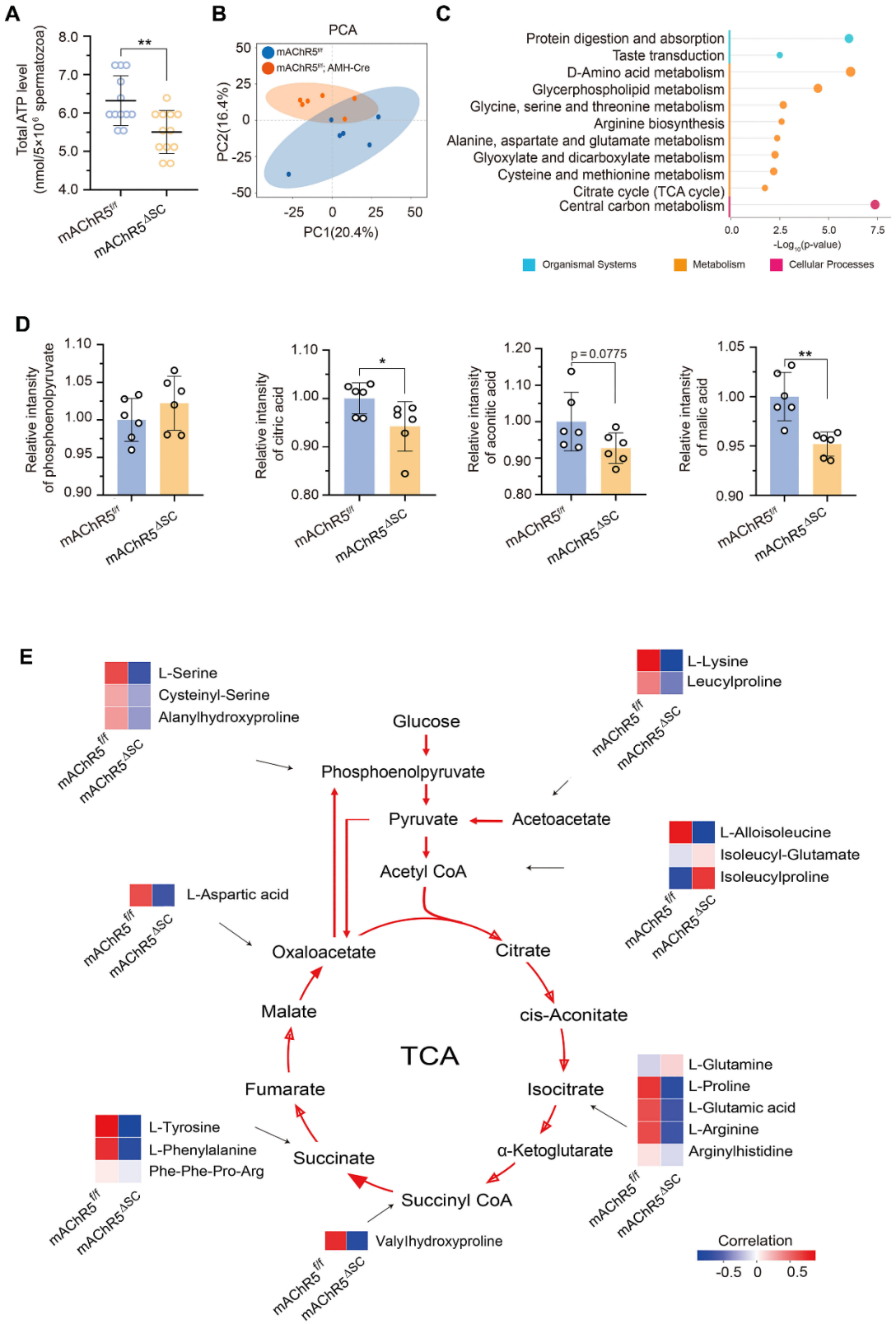


Figure 6. Metabolomic alterations in mouse spermatozoa. (A) Total ATP levels in spermatozoa of mAChR5$^{f/f}$ and mAChR5$^{\Delta SC}$ mice. n = 12 per group. **(B)** Principal component analysis (PCA) of sperm metabolites. n = 6 per group. **(C)** Pathway

enrichment analysis of differentially abundant sperm metabolites. **(D)** Differential levels of tricarboxylic acid (TCA) cycle-related metabolites in spermatozoa. n = 6 per group. Mean ± s.d. *p < 0.05, **p < 0.01. **(E)** Untargeted sperm metabolomic profiling, highlighting differential expression of amino acids associated with the tricarboxylic acid (TCA) cycle.